# Spatiotemporal Koopman Decomposition of Plasma Forcing with a Serpentine Plasma Actuator

Arman C. Ghannadian[*], Ryan Gosse[†], and Subrata Roy[‡]
*University of Florida, Gainesville, Florida, 32611, USA*

**The spatiotemporal Koopman decomposition (STKD) is a data-driven modal decomposition technique that provides a means to represent a flow-field as a sum of standing and traveling waves with temporal and spatial growth rates. The method involves repeated application of dynamic mode decomposition (DMD) or higher-order DMD (HODMD). In this paper, HODMD and STKD are shown to be useful in analyzing coherent structures in a flow-field perturbed by a square serpentine plasma actuator. The methods are applied to an implicit large eddy simulation (ILES) run with our in-house CFD code Multiscale Ionized Gas (MIG) which modeled a square-serpentine plasma actuator on a flat plate at Mach 0.5 to cause transition. Previous work performed a proper orthogonal decomposition (POD) for this type of actuation to analyze the relative energy content of various modes. The STKD allows for tracking the spatiotemporal growth of the generated flow structures before transition, providing more detail about the process leading up to transition.**

## I. Nomenclature

| | | |
|---|---|---|
| $a$ | = | HODMD/STKD mode amplitude |
| $d$ | = | Delay parameter |
| $I, J, K$ | = | Number of data points along spatial dimensions |
| $P_1, P_2, P_3$ | = | HOSVD mode matrices reduced rank |
| $S$ | = | Core tensor |
| $u$ | = | HODMD/STKD mode shapes |
| $\mathcal{V}$ | = | Snapshot matrix/tensor |
| $x, y, z$ | = | Spatial dimensions |
| $t$ | = | Time |
| $T, X, Z$ | = | HOSVD mode matrices |
| $\delta$ | = | Temporal growth rate |
| $\tau_w$ | = | Wall shear stress |
| $\omega$ | = | Angular frequency |
| $\kappa$ | = | Angular wavenumber |

## II. Introduction

Transition prediction and control is a vital area of research for many flow regimes due to key differences in drag and heat transfer between turbulent and laminar flows. Many characteristics of transitional flows and methods for controlling transition elude investigators. The nonlinearity of the problem means that certain types of analyses, e.g. linear stability theory (LST) [1] or parabolized stability equations (PSE) [2] can only provide information for part of the flow-field. Generally, high-fidelity computational fluid dynamics (CFD) simulations or experiments are required for more detailed analyses. Once data is obtained, either from CFD or experiment, many post-processing techniques can be applied to gain a deeper understanding of the flow physics. In addition to usual flow-variable calculation and statistics, data-driven modal analysis techniques can provide valuable insight.

---

*[*]PhD Student, Department of Mechanical and Aerospace Engineering, AIAA Student Member.ghannadian.arman@ufl.edu*
*[†]Professor of Practice, Florida Applied Research in Engineering, AIAA Associate Fellow. ryan.gosse@ufl.edu*
*[‡]Professor, Department of Mechanical and Aerospace Engineering, AIAA Associate Fellow. roy@ufl.edu*

The various data-driven modal decomposition methods are ways of analyzing complex system dynamics via decomposing a data set into a sum of modes. These modes may correspond to some physical mechanism in the flow or a coherent structure of interest. The dynamic mode decomposition (DMD) and the proper orthogonal decomposition (POD) are two of the most widely used decompositions, and there are many extensions and variants of these [3–5]. The POD computes orthogonal modes that optimally capture the variance of the data. In this paper, we refer to the spatial POD commonly known as the snapshot POD developed in [6], which can differ significantly from Lumley's original formulation [7, 8]. This is because the DMD can be considered as an extension of the snapshot POD. The connection between the DMD and the POD is the singular value decomposition (SVD), a general matrix decomposition that can be directly applied to the (mean-subtracted) snapshot matrix to yield POD modes [5, 9]. DMD is performed by computing the best-fit operator that advances snapshots of data one time step into the future to compute single-frequency modes, and the regression may be done after first projecting onto the leading SVD modes as a way to filter noise (which is decomposed into low-variance SVD modes).

Although the DMD modes have linear dynamics (complex exponentials), their use for analyzing nonlinear systems is justified via the connection to the Koopman operator: a linear operator that acts on measurement functions of a nonlinear system whose spectral decomposition characterizes the nonlinear system [10]. The focus of this paper is applying extensions of DMD that overcome the limitations of standard DMD and the rank-reduction via the truncated POD to a simulation of plasma forcing on a flat plate to analyze the mechanisms by which the actuation was able to bring about transition to turbulence. A similar case was previously analyzed with snapshot POD to examine the relative energy content of various modes undergoing plasma forcing [11]. The simulation was an implicit large eddy simulation (ILES) that used modal discontinuous Galerkin (DG) spatial discretization with the Multiscale Ionized Gas (MIG) code [12] to solve the compressible Navier-Stokes equations. The plasma forcing was modeled by a body force approximation based on the model in [13] to generate the 3D structures known to result from serpentine actuators [14]. The effects of actuator collocation have been investigated with POD as well [15]. This gave fundamental insight into how serpentine-style actuators can be used for low-speed transition control via manipulating 3D boundary layer instability mechanisms [16]. The non-collocated (one actuator) case is the focus of this investigation. It is known that the actuation generates staggered pairs of lambda vortices, which ultimately interact and lead to oblique wave transition [11]. Therefore, it was desirable to investigate this flow-field by isolating frequency and wavenumber to capture the spatiotemporal growth of the perturbations. This is the benefit of DMD-like methods — they allow users to isolate modes that have fixed frequency and associated exponential growth. Figure 1 below shows a contour of $u$-velocity from the data set for Mach 0.5 flow over a flat plate. Figure 2 shows isosurfaces of Q-criterion colored by $u$-velocity. The influence of the actuator at the leading edge is clear, and the flow can be seen to breakdown to turbulence farther downstream.
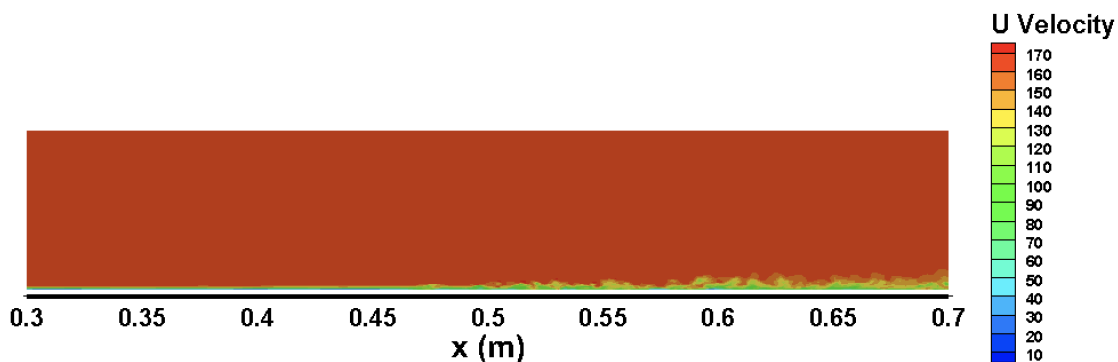


**Fig. 1   Contour of $u$-velocity.**

The Spatiotemporal Koopman decomposition (STKD) [17] takes the benefits of DMD a step further by computing modes that are traveling waves with fixed spatial wavenumber, temporal frequency, and spatial and temporal growth/decay rates. Since its development, the STKD has been applied to study offshore wind turbines [18, 19], arch vortices in urban flows [20], reconstructing 3D flow-fields from 2D data sets [21], and also for extracting growth rates of pixel value from experimental schlieren (which is related to density gradient) depicting second mode instability waves on hypersonic cone geometries [22]. As discussed later in the paper, isolating based on wavenumber is not always the best method since spatially stretching waves will result in many wavenumbers (modes) representing a single coherent structure
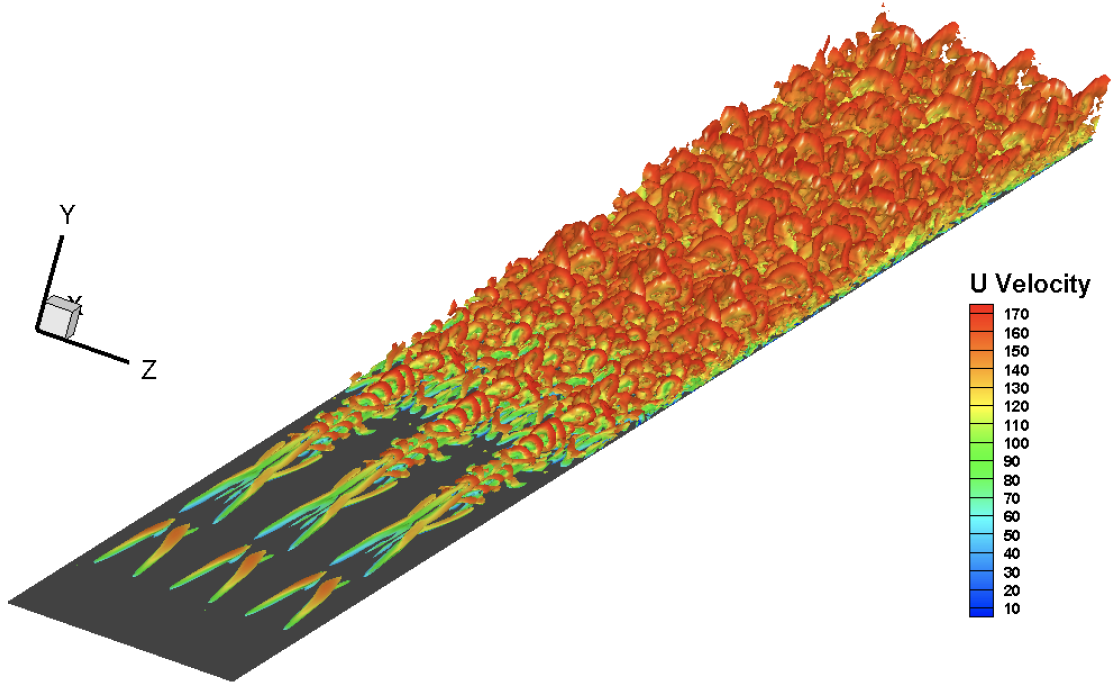
2

**Fig. 2    Isosurfaces of Q-criterion colored by $u$-velocity.    The domain duplicated twice to show 3 spanwise wavelengths of the actuator.**

evolving. Regardless, the STKD will provide the most dominant wavenumbers for a given frequency. This provides a general size and quantified spatial growth rates of various structures in the flow-field. This is advantageous for analyzing spatially developing flows or convective instabilities, for example. A similar spatiotemporal decomposition can be performed with the original Lumley decomposition for POD where homogeneous directions and temporal stationarity require harmonic decompositions [7, 8, 23, 24]. A key difference with the STKD is the potential for growth rates in the direction that is transformed into the frequency or wavenumber domain. Thus, the STKD can capture intensifying traveling waves. Of course, doing a Fourier transform in time (spectral POD [25]) can produce good results due to the strong connection between wavespeed, temporal frequency, and wavenumber. A small drawback of HODMD is that it can lump together waves of different wavespeeds into a single mode if the wavenumber is such that they have the same frequency of occurrence. However, the STKD guarantees this decomposition into waves with fixed distinct wavenumbers and frequency. The largest benefit of the STKD is that it directly and efficiently computes growth rates in addition to wavenumbers.

The basic form of DMD and its higher-order extension used in this paper which can be more robust for data exhibiting high spectral complexity, higher-order DMD (HODMD) [26], both decompose a snapshot matrix $\mathcal{V}_{ik} = \mathcal{V}(\mathbf{x}_i, t_k)$ as the following Fourier expansion:

$$\mathcal{V}_{ik} = \sum_{n=1}^{N} a_n u_{in} e^{(\delta_n + i\omega_n)t_k}. \tag{1}$$

Here, the $\mathbf{x}$ is a vector containing all spatial points in the domain, $a_n$ are DMD mode amplitudes, $u_{in}$ are the generally complex-valued DMD modes, $\delta_n$ are the temporal growth rates of each mode, and $\omega_n$ are the angular frequencies at which each mode oscillates. The HODMD obtains this expansion by making the higher order Koopman assumption

$$\mathbf{v}_{k+d} = R_1\mathbf{v}_k + \mathbf{v}_{k+1} + ... + R_d\mathbf{v}_{k+d-1}, \tag{2}$$

for $k = 1, ..., K - d$. If the delay parameter $d$ equals one, then the method is the same as standard DMD. Thus, this assumption is the more general way of obtaining the expansion in Eq. 1 than the commonly applied standard DMD

3

assumption. Increasing $d$ increases the rank of the snapshots used, and the rank limits the number of modes with nonzero eigenvectors. This affects the quality of DMD results when a dimension reduction via truncated SVD has been performed to remove noise or when the data is spatially undersampled. Taken's delay embedding theorem justifies performing a dimension reduction followed by augmenting the reduced snapshots with delayed snapshots [26]. One HODMD mode oscillating at different frequencies $\omega$ can be a spatial function with multiple wavenumbers $\kappa$ and therefore be made up of many different wave speeds $c$, where $c = -\omega/\kappa$. The data may also be organized as a higher-order snapshot tensor with each dimension corresponding to a different index of the tensor rather than a 2D matrix. The snapshot tensor is represented for 3D unsteady data as $\mathcal{V}_{ijrk} = \mathcal{V}(x_i, y_j, z_r, t_k)$. In this case, an HOSVD can be a first step rather than a standard SVD. The DMD algorithm is then applied to the temporal modes that result (for more details, see Appendix Alg.1). It should be noted that this method is equivalent to the standard SVD-based DMD if no truncation is done on the HOSVD spatial mode matrices, a step that allows for additional filtering in each dimension.

The STKD method expands a snapshot tensor (of any number of dimensions, but 2D is detailed here) $\mathcal{V}_{ijk}$ as

$$\mathcal{V}_{ijk} = \sum_{m=1}^{M} \sum_{n=1}^{N} a_{mn} u_{mn}(z_k) e^{(\nu_m + i\kappa_m)x_i + (\delta_n + i\omega_n)t_k}, \tag{3}$$

or any similar variant. For example, $z$-direction wavenumber could be desirable instead of $x$, or both $x$ and $z$ could appear only in the complex exponential and the STKD mode shapes could be only functions of $y$ in 3D. However, for this study, the expansion in Eq. 3 is the desired form.

This paper proceeds as follows. A quick overview of the setup and methodology that was implemented for the multi-dimensional HODMD as well as the STKD is presented. The algorithms are given more detail in the Appendix. Next, results showing an HODMD analysis of the flow are given. These results show the flow response to actuation with the growth of higher harmonic modes. Finally, results from the STKD analysis detailing dominant wavenumbers and associated growth rates are presented and interpreted.

## III. Methodology

There are a large number of variants of DMD-based methods, but many present issues when capturing transient dynamics [10]. We explore the use of HODMD with delay embedding to obtain expansions with the STKD. Various forms of Eq.3 are obtainable, and the algorithm differs slightly depending on the exact form. Therefore, it is important to describe the steps taken in the present study. Brief overviews of the algorithms for multi-dimensional HODMD [27], DMD-$d$ (the key algorithm for HODMD)[26], and STKD [17] are given in the Appendix in Algs.1, 2, and 3 for completeness and clarity. For a detailed description and derivation of the methods, see [17, 26–28].

For the temporal HODMD, $\tau_w$ was analyzed as a simple way of determining the effects of actuation by taking 2D slices of data along the wall, since velocity gradients succinctly describe the nonlinear dynamics of the flow [29]. The DMD has been applied similarly to the skin friction coefficient in an analysis of H-type transition [30], in which staggered pairs of lambda vortices interact to cause transition similar to the present case. In addition, the data set was cropped before analysis to only include the region just before transition started. The purpose of this was to most clearly quantify the effects of actuation leading up to transition without being hindered by the increased complexity of the flow-field downstream. As will be seen below, useful insights into the lead-up to transition are obtained even with this spatial truncation. A total of 783 snapshots were used with $\Delta t = 20 \, \mu$s, or a sampling frequency of 50 kHz. This allows for the actuation frequency of 2 kHz to cycle 31.28 times. In other words, if $T = 2\pi/\omega_{act}$ then the time interval sampled is $31.28 \, T$. A simulation with the setup from [11] was run longer to enable the post-processing of more time steps to build a longer time series at a high sampling rate. The tolerance parameter $\epsilon$ was set to $1 \times 10^{-4}$ for HOSVD, SVD, and amplitude truncations. A delay parameter of $d = 80$ was used.

The STKD analysis also used $\tau_w$ snapshots. However, the mean was subtracted before application so that traveling waves were better captured. Due to this, the tolerances were set for a slightly heavier rank truncation of $5 \times 10^{-3}$. In addition, the flow-field was cropped to not include the actuator. Including the actuator resulted in a large number of modes which only represented small, quickly decaying perturbations that remained in the immediate vicinity of the actuator. Additionally, only 301 snapshots were used in this analysis. This was more than enough to obtain the same dominant frequencies, and it captures 12 periods of actuation frequency of 2 kHz. Since fewer snapshots were used, a delay parameter of $d = 30$ was used in time. For the spatial dimension, a delay parameter of $d = 2$ minimized the reconstruction error for the given $\varepsilon$ tolerance.

# IV. Results and Discussion

## A. HODMD Temporal Analysis

In this section, we present results for HODMD temporal analysis of the data. The normalized amplitudes (normalized by maximum amplitude) are plotted against frequency in Fig. 3a. The real and imaginary components of the eigenvalues for each mode are given in Fig. 3b. The real parts of the first 6 mode shapes are given in Fig. 4.
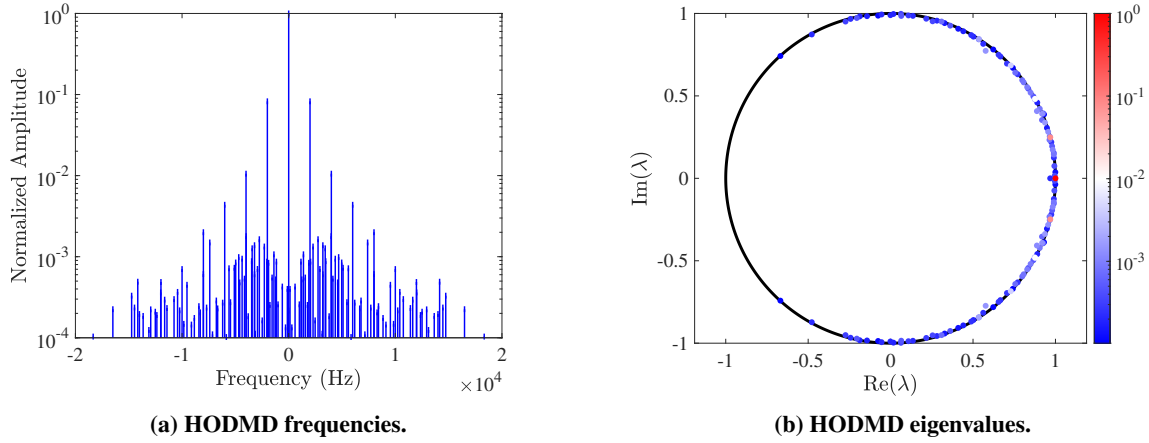


**(a) HODMD frequencies.**



**(b) HODMD eigenvalues.**

**Fig. 3    HODMD spectrum.**



**(a) HODMD mode 1.**



**(b) HODMD mode 2 (2 kHz).**



**(c) HODMD mode 3 (4 kHz).**



**(d) HODMD mode 4 (6 kHz).**



**(e) HODMD mode 5 (8 kHz).**



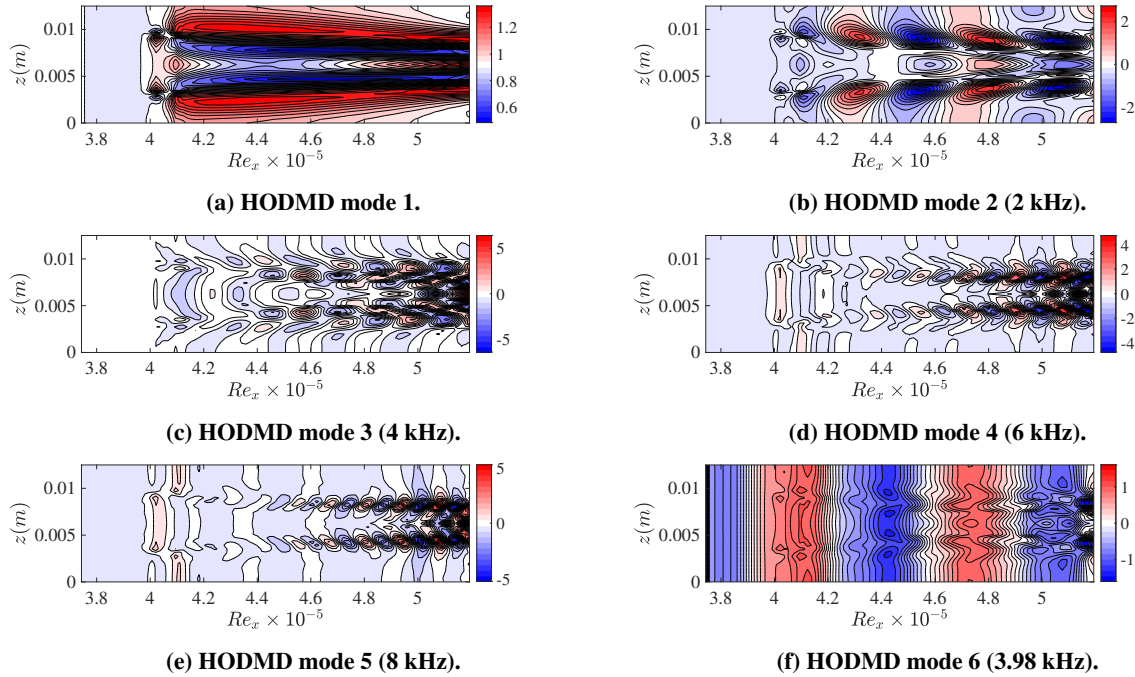**(f) HODMD mode 6 (3.98 kHz).**

**Fig. 4    HODMD mode contours.**

In Fig. 4 above, the modes are ranked according to the amplitudes solved for via a least-squares best fit. Note that the true value on the color bar is less significant than the change from negative to positive. This is because all modes have the same Frobenius norm. Therefore, the best way to discern the relative importance of modes is by the amplitude plot (Fig. 3a). As can be seen in Fig. 3a, there are clusters of modes around the dominant frequencies that have relatively

5

high amplitudes. For that reason, although modes 3,4 and 5 are harmonics of the primary actuation frequency, the next few modes do not show higher harmonics of the actuation frequency. This is already evident with mode 6 in Fig. 4f which is close to the frequency of mode 3 and not a harmonic of the main actuation frequency. Many of the modes in between the main harmonics are similar to mode 6 in appearance. For this reason, below in Fig. 5 are plotted modes 23, 36, and 56, which correspond to 10 kHz, 12 kHz, 14 kHz, respectively. All of these modes show intensification in the downstream direction. In addition to that, it is clear that the main mode structures of each harmonic mode originate farther downstream than those of the previous harmonic. There is a dominant pattern intensifying in the streamwise direction and this motivates further decomposition via STKD to quantify the dominant growth rates and wavenumbers.
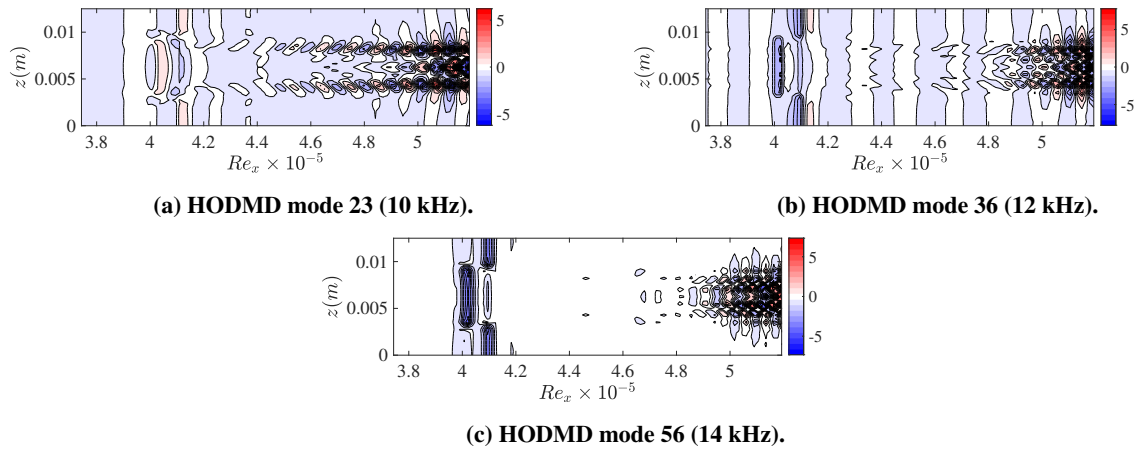


(a) HODMD mode 23 (10 kHz).



(b) HODMD mode 36 (12 kHz).



(c) HODMD mode 56 (14 kHz).

**Fig. 5   HODMD mode contours corresponding to higher harmonics of actuation frequency.**

## B. Spatiotemporal Analysis

The lambda structures generated by the actuator forcing mechanism stretch as they travel in the streamwise direction. This results in a high spectral complexity in $x$. In other words, the dominant modes have wavenumbers which are decreasing as they convect downstream. Since STKD finds single wavenumber modes, these structures will be represented by several modes with different wavenumbers and wavespeeds. This can increase the complexity of interpretation of the resulting modes, because many STKD modes are required to represent a single flow structure, which is the stretching lambda vortex. Nonetheless, the main flow features are identified by the largest amplitude waves and the only complication that will arise is additional waves at similar frequencies and wavenumbers and slightly faster or slower wavespeeds.

It is clear from looking at a space-time diagram along any constant $z$ line that the flow is dominated by a single traveling wave. This corresponds to the primary pairs of lambda vortices traveling downstream as can be seen in Fig. 2 and is also evident in the second HODMD temporal mode in Fig. 4b. Figure 6a shows the spacetime diagram along the centerline. The slope $dx/dt$ for a given structure in the diagram is the wavespeed. This value changes slightly in the streamwise direction, which also explains the large number of modes obtained. Figure 6b shows the reconstruction of Fig. 6a with the STKD modes and the tolerances described in Sec. III. With these tolerances, 70 spatiotemporal modes were kept. There is good agreement qualitatively, and a better agreement could have been obtained by keeping more modes. However, the reconstruction based on these modes captures the state of the system reasonably.
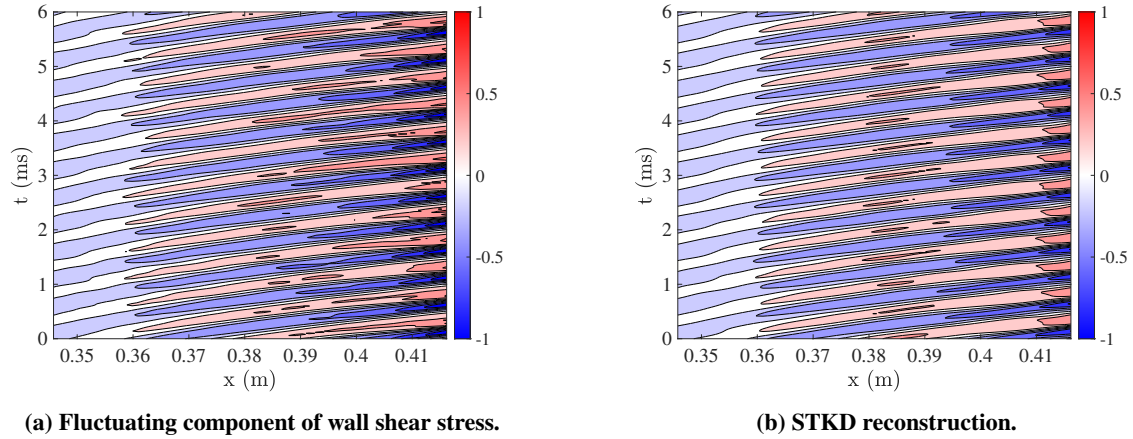
6

**(a) Fluctuating component of wall shear stress.**



**(b) STKD reconstruction.**

**Fig. 6   STKD reconstruction of wall shear stress fluctuations along centerline ($z = 6.25$ mm).**

The main results of the spatiotemporal analysis are spatial growth rates for a given wavenumber. In addition, the speed of various waves can be obtained by examining a dispersion diagram. As shown in Fig. 3a, the HODMD modes with harmonic frequencies of the actuator frequency have amplitudes that drop off in magnitude very rapidly. Similarly, the dominant STKD modes are associated with the 2 kHz mode and its harmonics. In the dispersion diagram in Fig. 7a below, the 70 modes (35 complex conjugate pairs) are scattered. The wavespeed is the negative of the slope of the lines connecting the complex conjugate eigenvalues. Many of the dominant modes have positive wavespeed. However, some lower-amplitude waves are propagating upstream. These waves have positive growth in the streamwise direction, so they decay exponentially as they propagate upstream. In addition, Fig. 7b shows that all of the STKD modes have positive growth rates in the streamwise direction. Notably, the highest spatial growth rate is attributed to the primary actuation frequency and its harmonics.
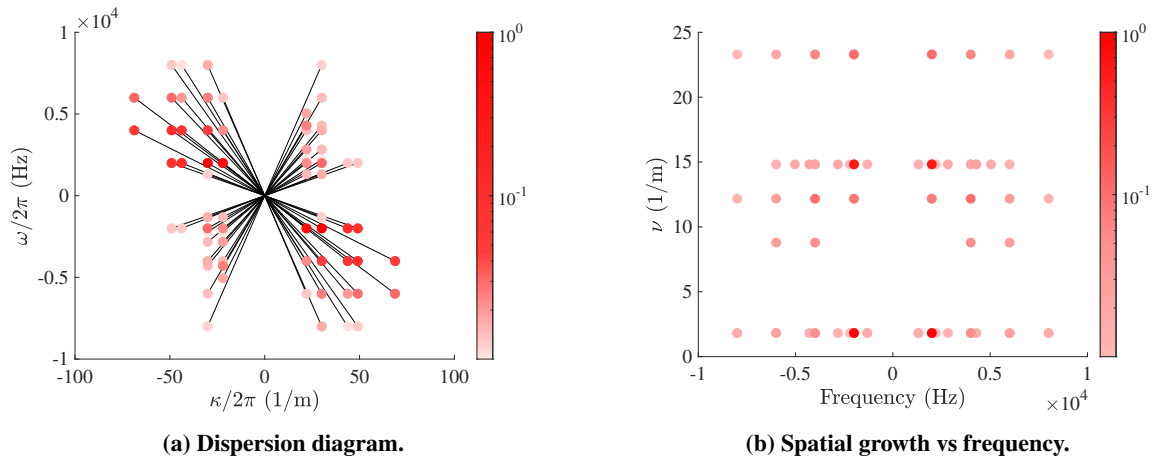


**(a) Dispersion diagram.**



**(b) Spatial growth vs frequency.**

**Fig. 7   Dispersion diagram and spatial growth rates. The colormap represents normalized mode amplitude.**

The primary actuation frequency contains 4 traveling waves in the positive $x$ direction with growth rates of $\nu = 1.82, 14.82, 12.17$, and $23.29$. The largest amplitude modes have the primary actuation frequency and these growth rates. In addition, the waves with a negative wavespeed at this frequency have the same growth rate. The reconstruction of these opposing waves in time gives a single traveling wave for each wavenumber active at 2 kHz growing in $x$ non-uniformly. The reconstructed wave has a magnitude that increases in $x$, then pauses momentarily and then increases in $x$ more, and so on. The wavespeed also undulates slightly. This effect is small, though, due to the differences in amplitudes. For example amplitudes $a_{3,2}$ and $a_{4,1}$ which correspond to a downstream propagating dominant wave are 25.66 times higher than $a_{3,1}$ and $a_{4,2}$ (the corresponding upstream propagating wave with the same wavenumber and

7

frequency). However, this effect is important to note since it means that some of the upstream propagating waves are not necessarily flow structures but rather manifestations of non-uniform growth of the primary waves in the streamwise direction. This could correspond to the forcing pattern of the actuator, which in time takes the form of the absolute value of a sine wave, and also the cyclic interactions of the pairs of lambda vortices.

## V. Conclusions and Future Work

We have presented a DG-ILES simulation of flow turbulization using a body force simulating a square-serpentine plasma actuator. Results for a temporal HODMD applied to the $\tau_w$ field are given. The HODMD modes show the primary structures generated by the forcing mechanism, and higher modes show higher harmonics of this frequency. STKD was used to represent the mean-subtracted data set as a sum of traveling waves. This allowed wavenumbers and spatial growth rates to be computed in addition to temporal frequencies. The STKD results in a large number of dominant modes, so further cropping of the domain in addition to higher truncations of rank in each direction via HOSVD was required. The modes with the primary actuation frequency of 2 kHz and harmonics of this frequency were dominant and had the highest spatial growth rates. Several upstream propagating waves resulted from the analysis as well. However, reconstructing based on counter-propagating waves showed that some of the upstream propagating waves (particularly those at 2 kHz) were not true flow features, but rather a result of non-uniform growth of the primary 2 kHz structures. The reconstructed wave grows in $x$, pauses, and continues to grow in $x$ cyclically. Future work will involve application further into the transitional regime of the flow where the high spectral complexity in both the streamwise direction and time will result in more difficulty in isolating the actuator's effects. Ultimately, various expansions similar to Eq. 3 could prove to be more useful, and this will be explored as well. Finally, the STKD could be used to examine different flow/actuator configurations, such as frequency, spanwise wavenumber, or freestream conditions, to determine how these variables affect the growth rates of the various modes.

## Appendix

---

**Algorithm 1** Multidimensional HODMD

---

1: Organize the data as a snapshot tensor:

$$\mathcal{V}_{ijk} = \mathcal{V}(x_i, z_j, t_k). \tag{4}$$

2: Apply a truncated HOSVD as

$$\mathcal{V}_{ijk} = \sum_{p_3=1}^{P_3} \sum_{p_2=1}^{P_2} \sum_{p_1=1}^{P_1} S_{p_1 p_2 p_3} X_{i p_1} Z_{j p_2} T_{k p_3}, \tag{5}$$

where $S_{p_1 p_2 p_3}$ is the *core tensor*. The exact number of kept HOSVD modes ($P_1$, $P_2$, $P_3$) can be determined based on limiting the rank when singular values drop below some tolerance. For this paper $\sigma/\sigma_1 >= \varepsilon$ was used for all directions.

3: Multiply each row of the transpose of the temporal mode matrix $T_{p_3 k}$ by its associated singular values:

$$\hat{T}_{p_3 k} = \sigma^t_{p_3} T_{p_3 k}. \tag{6}$$

4: Apply the DMD-*d* algorithm to the above *reduced snapshots*, resulting in:

$$\hat{T}_{p_3 k} \approx \sum_{n=1}^{N} a^t_n u^t_{p_3 n} e^{(\delta_n + i \omega_n) t_k}. \tag{7}$$

5: Construct the full modes by plugging $\sigma^t_{p_3} u^t_{k p_3}$ into the HOSVD expansion in place of $T_{k p_3}$. Note that the *reduced mode* matrix is transposed here.

6: Normalize the modes to have unit RMS norm and scale the amplitudes accordingly.

---

8

---

**Algorithm 2** DMD-d Alogrithm

---

1: The *higher-order Koopman assumption* is applied to rescaled temporal modes matrix as

$$\hat{T}_{d+1}^K \approx \hat{R}_1 \hat{T}_1^{K-d} + \hat{R}_2 \hat{T}_2^{K-d+1} + ... + \hat{R}_d T_d^{K-1}, \tag{8}$$

where $R_n$ are matrices. For matrices with a superscript and a subscript, the notation denotes the columns of the matrix. For example, $T_1^4$ denotes the first four columns of the $T$ matrix.

2: Form the *modified snapshot matrix* $\tilde{T}$ as where each column of $\tilde{T}$ is given as

$$\tilde{\mathbf{t}}_k = \begin{bmatrix} \hat{\mathbf{t}}_k \\ \hat{\mathbf{t}}_{k+1} \\ ... \\ \hat{\mathbf{t}}_{k+d-1} \end{bmatrix}, \tag{9}$$

for $k = 1, ..., K - d + 1$. Note that $\hat{\mathbf{t}}$ are the columns of the rescaled temporal mode matrix $\hat{T}$.

3: Apply a truncated SVD to the *modified snapshots* as

$$\tilde{T} = U\Sigma V^T, \tag{10}$$

keeping the leading SVD modes by truncating based on the tolerance $\varepsilon$ as described above for the HOSVD.

4: Define the *reduced modified snapsnots* as

$$\bar{T} = \Sigma V^T. \tag{11}$$

5: Apply the *higher order Koopman assumption* to the *reduced modified snapsnots* as

$$\bar{T}_2^{K-d+1} = \bar{R} \bar{T}_1^{K-d}. \tag{12}$$

6: Solve for the least-squares solution for $\bar{R}$. The eigenvalues of this matrix are the HODMD eigenvalues $\lambda_n$. The growth rate and angular frequency (or wavenumber) are the real and imaginary parts of $\ln(\lambda_n)/\Delta t$, respectively.

7: Calculate the *reduced modes* as the first $P_3$ components of each column $U\bar{\phi}$, where $\bar{\phi}$ are the eigenvectors of $\bar{R}$.

8: Solve for the amplitudes $a_n^t$ via regression of the expansion to the *reduced snapshots* $\hat{T}$.

---

**Algorithm 3** STKD Algorithm

---

1: Apply steps 1 to 4 of the Multi-Dimensional HODMD algorithm outlined above.

2: Apply the DMD-*d* algorithm to a spatial matrix whose dynamics are of interest (scaled by the singular values), resulting in

$$\hat{X}_{p_1 i} = \sigma_{p_1}^x X_{p_1 i}, \tag{13}$$

and

$$\hat{X}_{p_1 i} \approx \sum_{m=1}^M a_m^x \hat{u}_{p_1 m} e^{(\nu_m + i\kappa_m)x_i}. \tag{14}$$

3: Now solve for the non-normalized modes $\tilde{u}_{jmn}$ as

$$\tilde{u}_{jmn} = a_m^x a_n^t \sum_{p_1=1}^{P_1} \sum_{p_3=1}^{P_3} \hat{S}_{p_1 j p_3} u_{p_1 m}^x u_{p_3 n}^t, \tag{15}$$

where

$$\hat{S}_{p_1 j p_3} = \frac{1}{\sigma_{p_1}^x \sigma_{p3}^t} \sum_{p_2=1}^{P_2} S_{p_1 p_2 p_3} Z_{j p_2}. \tag{16}$$

4: Solve for the STKD amplitudes $a_{mn}$ as the Frobenious norm of each mode divided by $\sqrt{J}$, and divide $\tilde{u}_{jmn}$ by these amplitudes so the final modes $u_{jmn}$ have unit RMS norm.

---

9

## Acknowledgments

## References

[1] Mack, L. M., "Boundary-Layer Linear Stability Theory," Tech. Rep. 709, NATO Advisory Group for Aerospace Research and Development (AGARD), 1984. AGARD Report No. 709.

[2] Herbert, T., "PARABOLIZED STABILITY EQUATIONS," *Annual Review of Fluid Mechanics*, Vol. 29, No. 1, 1997, p. 245–283. https://doi.org/10.1146/annurev.fluid.29.1.245, URL http://dx.doi.org/10.1146/annurev.fluid.29.1.245.

[3] Begiashvili, B., Groun, N., Garicano-Mena, J., Le Clainche, S., and Valero, E., "Data-driven modal decomposition methods as feature detection techniques for flow problems: A critical assessment," *Physics of Fluids*, Vol. 35, No. 4, 2023. https://doi.org/10.1063/5.0142102, URL http://dx.doi.org/10.1063/5.0142102.

[4] Schmid, P. J., "Dynamic Mode Decomposition and Its Variants," *Annual Review of Fluid Mechanics*, Vol. 54, No. 1, 2022, p. 225–254. https://doi.org/10.1146/annurev-fluid-030121-015835, URL http://dx.doi.org/10.1146/annurev-fluid-030121-015835.

[5] Taira, K., Brunton, S. L., Dawson, S. T. M., Rowley, C. W., Colonius, T., McKeon, B. J., Schmidt, O. T., Gordeyev, S., Theofilis, V., and Ukeiley, L. S., "Modal Analysis of Fluid Flows: An Overview," *AIAA Journal*, Vol. 55, No. 12, 2017, p. 4013–4041. https://doi.org/10.2514/1.j056060, URL http://dx.doi.org/10.2514/1.J056060.

[6] Sirovich, L., "Turbulence and the dynamics of coherent structures. I. Coherent structures," *Quarterly of Applied Mathematics*, Vol. 45, No. 3, 1987, p. 561–571. https://doi.org/10.1090/qam/910462, URL http://dx.doi.org/10.1090/qam/910462.

[7] Lumley, J. L., *Stochastic Tools in Turbulence*, Dover Publications, New York, 2007.

[8] Singh, S., and Ukeiley, L., "Proper Orthogonal Decomposition of High-Speed Particle Image Velocimetry in an Open Cavity," *AIAA Journal*, Vol. 58, No. 7, 2020, p. 2975–2990. https://doi.org/10.2514/1.j059046, URL http://dx.doi.org/10.2514/1.J059046.

[9] Weiss, J., "A Tutorial on the Proper Orthogonal Decomposition," *AIAA Aviation 2019 Forum*, American Institute of Aeronautics and Astronautics, 2019. https://doi.org/10.2514/6.2019-3333, URL http://dx.doi.org/10.2514/6.2019-3333.

[10] Brunton, S. L., Budišić, M., Kaiser, E., and Kutz, J. N., "Modern Koopman Theory for Dynamical Systems," *SIAM Review*, Vol. 64, No. 2, 2022, p. 229–340. https://doi.org/10.1137/21m1401243, URL http://dx.doi.org/10.1137/21M1401243.

[11] Gupta, A. D., and Roy, S., "Three-dimensional plasma actuation for faster transition to turbulence," *Journal of Physics D: Applied Physics*, Vol. 50, No. 42, 2017, p. 425201. https://doi.org/10.1088/1361-6463/aa8879, URL http://dx.doi.org/10.1088/1361-6463/aa8879.

[12] Houba, T., Dasgupta, A., Gopalakrishnan, S., Gosse, R., and Roy, S., "Supersonic turbulent flow simulation using a scalable parallel modal discontinuous Galerkin numerical method," *Scientific Reports*, Vol. 9, No. 1, 2019. https://doi.org/10.1038/s41598-019-50546-w, URL http://dx.doi.org/10.1038/s41598-019-50546-w.

[13] Singh, K. P., and Roy, S., "Force approximation for a plasma actuator operating in atmospheric air," *Journal of Applied Physics*, Vol. 103, No. 1, 2008. https://doi.org/10.1063/1.2827484, URL http://dx.doi.org/10.1063/1.2827484.

[14] Durscher, R. J., and Roy, S., "Three-dimensional flow measurements induced from serpentine plasma actuators in quiescent air," *Journal of Physics D: Applied Physics*, Vol. 45, No. 3, 2012, p. 035202. https://doi.org/10.1088/0022-3727/45/3/035202, URL http://dx.doi.org/10.1088/0022-3727/45/3/035202.

[15] Das Gupta, A., and Roy, S., "Modification of energetic modes for transitional flow control," *AIP Advances*, Vol. 12, No. 3, 2022. https://doi.org/10.1063/5.0078083, URL http://dx.doi.org/10.1063/5.0078083.

[16] Klebanoff, P. S., Tidstrom, K. D., and Sargent, L. M., "The three-dimensional nature of boundary-layer instability," *Journal of Fluid Mechanics*, Vol. 12, No. 1, 1962, p. 1–34. https://doi.org/10.1017/s0022112062000014, URL http://dx.doi.org/10.1017/S0022112062000014.

[17] Clainche, S. L., and Vega, J. M., "Spatio-Temporal Koopman Decomposition," *Journal of Nonlinear Science*, Vol. 28, No. 5, 2018, p. 1793–1842. https://doi.org/10.1007/s00332-018-9464-z, URL http://dx.doi.org/10.1007/s00332-018-9464-z.

[18] Le Clainche, S., Mao, X., and Véga, J., "Spatio-temporal Koopman Decomposition in offshore wind turbines," *17th International Symposium on Transport Phenomena and Dynamics of Rotating Machinery (ISROMAC2017)*, Maui, United States, 2017. URL https://hal.science/hal-02419848.

[19] Le Clainche, S., Mao, X., and Vega, J. M., "New method to capture traveling waves in flow passing a wind turbine," *Wind Energy*, Vol. 22, No. 7, 2019, p. 922–931. https://doi.org/10.1002/we.2331, URL http://dx.doi.org/10.1002/we.2331.

[20] Martínez-Sánchez, , Lazpita, E., Corrochano, A., Le Clainche, S., Hoyas, S., and Vinuesa, R., "Data-driven assessment of arch vortices in simplified urban flows," *International Journal of Heat and Fluid Flow*, Vol. 100, 2023, p. 109101. https://doi.org/10.1016/j.ijheatfluidflow.2022.109101, URL http://dx.doi.org/10.1016/j.ijheatfluidflow.2022.109101.

[21] Pérez, J. M., Le Clainche, S., and Vega, J. M., "Reconstruction of three-dimensional flow fields from two-dimensional data," *Journal of Computational Physics*, Vol. 407, 2020, p. 109239. https://doi.org/10.1016/j.jcp.2020.109239, URL http://dx.doi.org/10.1016/j.jcp.2020.109239.

[22] Ghannadian, A. C., Gosse, R. C., Roy, S., Lawless, Z. D., Miller, S. A., and Jewell, J. S., "Spatiotemporal Koopman decomposition of second mode instability from a hypersonic schlieren video," *Physics of Fluids*, Vol. 36, No. 9, 2024. https://doi.org/10.1063/5.0226443, URL http://dx.doi.org/10.1063/5.0226443.

[23] Citriniti, J. H., and George, W. K., "Reconstruction of the global velocity field in the axisymmetric mixing layer utilizing the proper orthogonal decomposition," *Journal of Fluid Mechanics*, Vol. 418, 2000, p. 137–166. https://doi.org/10.1017/s0022112000001087, URL http://dx.doi.org/10.1017/S0022112000001087.

[24] George, W. K., "Insight into the dynamics of coherent structures from a proper orthogonal decomposition dy," *International seminar on wall turbulence*, 1988.

[25] Towne, A., Schmidt, O. T., and Colonius, T., "Spectral proper orthogonal decomposition and its relationship to dynamic mode decomposition and resolvent analysis," *Journal of Fluid Mechanics*, Vol. 847, 2018, p. 821–867. https://doi.org/10.1017/jfm.2018.283, URL http://dx.doi.org/10.1017/jfm.2018.283.

[26] Le Clainche, S., and Vega, J. M., "Higher Order Dynamic Mode Decomposition," *SIAM Journal on Applied Dynamical Systems*, Vol. 16, No. 2, 2017, p. 882–925. https://doi.org/10.1137/15m1054924, URL http://dx.doi.org/10.1137/15M1054924.

[27] Corrochano, A., D'Alessio, G., Parente, A., and Le Clainche, S., "Higher order dynamic mode decomposition to model reacting flows," *International Journal of Mechanical Sciences*, Vol. 249, 2023, p. 108219. https://doi.org/10.1016/j.ijmecsci.2023.108219, URL http://dx.doi.org/10.1016/j.ijmecsci.2023.108219.

[28] Groun, N., Villalba-Orero, M., Lara-Pezzi, E., Valero, E., Garicano-Mena, J., and Le Clainche, S., "Higher order dynamic mode decomposition: From fluid dynamics to heart disease analysis," *Computers in Biology and Medicine*, Vol. 144, 2022, p. 105384. https://doi.org/10.1016/j.compbiomed.2022.105384, URL http://dx.doi.org/10.1016/j.compbiomed.2022.105384.

[29] Johnson, P. L., and Wilczek, M., "Multiscale Velocity Gradients in Turbulence," *Annual Review of Fluid Mechanics*, Vol. 56, No. 1, 2024, p. 463–490. https://doi.org/10.1146/annurev-fluid-121021-031431, URL http://dx.doi.org/10.1146/annurev-fluid-121021-031431.

[30] Sayadi, T., Schmid, P. J., Nichols, J. W., and Moin, P., "Reduced-order representation of near-wall structures in the late transitional boundary layer," *Journal of Fluid Mechanics*, Vol. 748, 2014, p. 278–301. https://doi.org/10.1017/jfm.2014.184, URL http://dx.doi.org/10.1017/jfm.2014.184.